Proceedings of the 7th International Symposium on Cavitation
CAV2009 – Paper No. 137
August 17-22, 2009, Ann Arbor, Michigan, USA

An Examination of Thermal Modeling Affects on the Numerical Prediction of Large-Scale Cavitating Fluid Flows

Michael P. Kinzel
Penn State University
Applied Research Laboratory
State College, PA, USA

Jules W. Lindau
Penn State University
Applied Research Laboratory
State College, PA, USA

Robert F. Kunz
Penn State University
Applied Research Laboratory
State College, PA, USA

ABSTRACT

The importance of modeling thermal effects in cavitating-fluid is examined in the context of computational fluid dynamics. Simulations of cavitation in water are used to study the effects of thermal versus and pressure variations in the fluid properties, and their impact on predictions. These studies are extended to evaluate energy-conserving approaches compared to isothermal ones, to assess the underlying thermal models influence on the predicted cavities occurring in water. Results indicate that the thermal effects remain important, but only for specific applications that need high-frequency phenomena from the numerical simulation. Low-frequency measures, needed for loading analysis, appear to be relatively insensitive to thermal effects. Lastly, various thermally driven cavitation problems requiring energy-equation conservation are presented to display applications requiring such a formulation.

INTRODUCTION

Recent efforts to improve the simulation of large-scale, naturally cavitating-fluid flows have focused on incorporating additional physics into the modeling approaches. Many numerical schemes simulate cavitating flows using incompressible-flow assumptions, however, in reality cavitating-fluid flows are highly compressible in the mixture regions and where phase change occurs [4]. Furthermore, thermal fluctuations associated with the release of latent heat during phase change processes occur in these vaporous cavities. Such temperature changes alter the fluid properties and can potentially change the cavitating-fluid dynamics. In this work, we intend to assess when the aforementioned effects are important for simulating vaporous cavitation using a computational fluid dynamics (CFD) approach.

It is well known that cryogenic-cavitating fluid flows are highly sensitive to thermal effects. Such work is documented and studied by Stepanoff [1], Billet [2], Hord [3], Franc & Michel [4], along many other studies. Thermal cavities display a completely different character than those that are relatively insensitive to thermal effects (typical to water flows). Such thermal sensitivities introduce additional scaling laws, in addition to cavitation number scaling, that include free-stream conditions and thermal sensitivities of the fluid properties. The character of a thermal cavity, typically frothy in the stable regions, differs from that of the sheet-like cavities that occur otherwise. As thermal cavities are a result of large temperature changes, their occurrence is prevalent to low-density-ratio cavities amount of phase change, by mass, is relatively large in order to fill the cavity void. A direct result of this increased phase change is an increased temperature drop and corresponding thermal effects [4]. Detailed computational-based examinations of these effects, explored by Ahuja *et al.* [5], display that the frothy cavities directly correlate to the latent heat, rather than fluid-property sensitivities. In any case, the accurate accounting of latent-heat energy release is required for CFD simulations of thermal cavitation.

The thermal effects in cavitating-water flows tend to be less pronounced, however, the effects remain relevant. Experimental studies have examined such effects, Cervone *et al.* [14] for example, and associate cavitation-number scaling issues, in water, when the free-stream temperatures vary. In particular, at free-stream temperatures approaching the boiling temperatures, the frothy cavity behavior becomes present in cavitating-water flows. In terms of marine vehicles, these increased temperatures typically fall outside temperatures encountered by control surfaces or open propellers, but could be relevant to pumps, pump jets, etc. Other relevant applications include rocket-propulsion plume used to propel underwater vehicles, boiling off water, or underwater explosions. Although in many water applications thermal cavitation is not considered an issue, many cases arise where it becomes relevant.

In this work, our goal is to explore some of the impacts of energy conservation with in a numerical simulation. Our model formulation is applied to open literature experiments where in some cases, the effects show importance. Various models are assessed based on the energy equation and thermodynamic relations. Finally, detailed behavior is examined for such flows. These studies should yield insight regarding (1) what factors are important in these simulations, (2) when are these factors important, (3) what is the most efficient method for such simulations. The overall objective is to give some reference or guidance of which physical aspects of cavitation need to be considered for specific problems.

COMPUTATIONAL MODEL DESCRIPTION

In this section, the computational fluid dynamics (CFD) approach is described. This model is based on the algorithm developed by Lindau *et al.* [6], which is a homogenous-multiphase, all-Mach-number preconditioned solution algorithm with full-energy conservation.

Model Equations

The differential form of the computational model in Cartesian tensor notation is given in Eq. 1. The corresponding conservative variables, primitive variables, flux vectors, and source terms are defined in Eqs. 2-6. The term $\Gamma^p \frac{\partial Q}{\partial \tau}$ is a result of the Choi-Merkle, dual-time preconditioned approach [7].

$$\frac{\partial Q_c}{\partial t} + \Gamma^p \frac{\partial Q}{\partial \tau} + F_{j,j} - F^v_{j,j} = H \tag{1}$$

$$Q^T = \begin{bmatrix} p & u_j & T & \alpha_k \end{bmatrix} \tag{2}$$

$$Q_c^T = \begin{bmatrix} \rho & \rho u_j & e & \tilde{\rho}_k \alpha_k \end{bmatrix} \tag{3}$$

$$F_j = \begin{bmatrix} \rho u_j \\ \rho u_i u_j + p\delta_{ij} \\ u_j(e+p) \\ \tilde{\rho}_k \alpha_k u_j \end{bmatrix} \tag{4}$$

$$F_j^v = \begin{bmatrix} 0 \\ t_{ij} \\ u_i t_{ij} + \kappa_{m,t} \dfrac{\partial T}{\partial x_j} \\ 0 \end{bmatrix} \tag{5}$$

$$H^T = \begin{bmatrix} 0 & 0_i & 0 & \dot{\omega}_k \end{bmatrix} \tag{6}$$

This preconditioning relieves the natural decoupling between the physical momentum and continuity equations in low Mach number flow. Here, the methodology of Venkateswaran and Merkle [7] is applied to derive a pseudo-inviscid eigensystem. This eigensystem then, ideally, dominates convergence of the pseudo-time marching system. Using the dual time approach, time accurate solutions are obtained by marching in pseudo-time over each physical time step and driving the time accurate residual, of the discrete form of the physical equations, to a small value. Additional details of the preconditioning are available in Lindau *et al.*[6] or Li *et al.* [8].

The (column) vectors expressed in Eqn. 1 are defined in Eqs. 2-6. The first elemental equation (row) represents continuity of the mixture. The next two rows are momentum and energy equations for the mixture. These represent the homogenous form of the governing equations for multiphase flows.

Homogeneous Multiphase-Flow Model

The last element in the system of equations represented in Eqs. 1-6 represents individual species continuity equations. The subscript k denotes gaseous species, $k=1,...,N$, where N represents the number of gaseous species, including the vapor. The tilde above the density indicates that the quantity is defined by the rule of Amagat, i.e. considering the isolated constituent, rather than the mixture. In following equations, the subscript l is used to refer to the liquid phase, which appears explicitly through the mixture-mass conservation equation. Also, summation over the gas species, subscripted by k, is implied.

The mixture continuity is expressed in the first equation position. Here, the liquid mass is explicitly given and added into the mixture properties. The mixture density is defined based on the local volume average density as

$$\rho = \alpha_k \tilde{\rho}_k + \alpha_l \tilde{\rho}_l \tag{7}$$

The viscous stress tensor takes on the usual form.

$$t_{ij} = \mu_{m,t}\left(u_{i,j} + u_{j,i} - \delta_{ij} \frac{2}{3} u_{k,k} \right) \tag{8}$$

In Eq. 9, the remaining necessary mixture quantities are defined. The subscript m indicates a liquid-gas mixture quantity. The mixture viscosity and Prandtl number are computed based on a local volume average. The mixture specific heat, is computed based on a mass average.

$$\begin{aligned} \mu_t &= \frac{\rho C_\mu k^2}{\varepsilon} \\ \mu_m &= \alpha_l \mu_l + \alpha_k \mu_k \\ \mu_{m,t} &= \mu_m + \mu_t \\ \mathrm{Pr}_m &= \alpha_l \mathrm{Pr}_l + \alpha_k \mathrm{Pr}_k \\ C_{pm} &= Y_l C_{pl} + Y_k C_{pk} \\ \kappa_{m,t} &= \left(\frac{\mu_m}{\mathrm{Pr}_m} + \frac{\mu_t}{\mathrm{Pr}_t} \right) C_{pm} \end{aligned} \tag{9}$$

These mixture relations provide a full-energy-conserving from of the governing equations for a homogeneous multiphase flow.

Numerical Scheme

The computational algorithm is enhanced with numerical schemes that are well suited for the examined flows. A finite-volume solution approach is applied that uses an approximate form of the Roe-flux-difference splitting approach [9]. A principle benefit of Roe's approach is the automatic satisfaction of jump conditions across shocks and other physical interfaces. One drawback is the difficulty in obtaining true "Roe averaging" for mixture state equations. In this work, the arithmetic average of the primitive variables is used and the recommendations of Vinokur and Liu [10], and others are not applied. Nevertheless, numerical experiments suggest that errors tend to affect the stability of computations for high temperature and pressure ratio shocks, which is not represented in the present cavitating-fluid flows. Within the finite-volume representation, the cell-face primitive-variable interpolations are computed using a third-order-accurate upwind-biased van-Albada flux-limited MUSCL formulation [11]. The scheme is thus, formally 3rd order accurate. The inviscid linear system uses analytic Jacobians, while the viscous is based on numerical Jacobians. The resultant linear system is solved using a block-symmetric, Gauss-Seidel technique. Finally, the solver uses structured, overset meshes to incorporate complex geometry.

Turbulence Modeling

A two-equation, k-ε turbulence closure model enhanced with a Detached Eddy Simulation (DES) approach is employed. These are solved in a segregated manner, or isolated from the flow equations, and can be represented as:

$$\frac{\partial Q_T}{\partial t} + \frac{\partial F_j^T}{\partial x_j} = PROD - DEST \tag{10}$$

$$Q_T = \begin{bmatrix} \rho k \\ \rho \varepsilon \end{bmatrix} \tag{11}$$

$$F_j^T = \begin{bmatrix} \rho k u_j - \left(\mu_m + \frac{\mu_t}{\sigma_k}\right)\frac{\partial k}{\partial x_j} \\ \rho \varepsilon u_j - \left(\mu_m + \frac{\mu_t}{\sigma_\varepsilon}\right)\frac{\partial \varepsilon}{\partial x_j} \end{bmatrix} \tag{12}$$

$$PROD = \begin{bmatrix} P \\ C_1 P \frac{\varepsilon}{k} \end{bmatrix} \tag{13}$$

$$DEST = \begin{bmatrix} \rho \varepsilon F_{DES} \\ C_2 \rho \frac{\varepsilon^2}{k} \end{bmatrix} \tag{14}$$

In the context of the *k*-ε model given in Eqn. 14, a DES variant is obtained by defining a modified turbulence energy destruction term [12]. Otherwise, the term F_{DES} in Eqn. 15 is set equal to unity and does not affect the term:

$$\begin{aligned} \mathrm{F_{DES}} &\equiv \mathrm{MAX}\left[\frac{\mathrm{L_t}}{\mathrm{C_{DES}}\Delta}, 1\right] \\ \Delta &\equiv \mathrm{MAX}(\delta_x, \delta_y, \delta_z) \\ \mathrm{L_t} &\equiv \frac{\mathrm{k}^{3/2}}{\varepsilon} \end{aligned} \tag{16}$$

Using this rather settle modification a hybrid turbulence model is encapsulated. In regions where the grid resolution is coarse relative to the turbulent scales, for example near walls, the turbulence model behaves in a traditional manner (F_{DES}=1). In regions where the grid resolution can support the large-scale eddies (F_{DES}>1), the destruction of *k* is amplified, and the modeling of μ_t is effectively reverted to model subgrid-scale stresses as done in a large-eddy simulation methodology. This formulation has been argued as behaving similar to the Smagorinski model [12]. Although more modern and sophisticated approaches have been developed, they are yet to be considered and would be expected to be applied in a similar manner.

A wall-function approach, or a high-Reynolds number, turbulence modeling approach is used. In this work, we incorporate a wall function based on Spalding's boundary layer model. This approach is reasonable from the viscous sub layer, through to the log-region of the boundary layer. Such an approach is extremely useful for the multiphase flows of interest, where with the mixed air or water regions, the needed wall spacing can vary considerably.

Cavitation Modeling

The transfer of mass between liquid and vapor is handled with simple finite-rate relations given in Eq. 17 and appears in the source term vector, Eq. 6, via definition of $\dot{\omega}_l = -(\dot{m}^+ + \dot{m}^-)$. The source term is further modified in the presence of chemical reactions.

$$\dot{m}^- = \frac{C_{dest}\tilde{\rho}_v \alpha_l MIN[0, p - p_v]}{\frac{1}{2}\rho_\infty U_\infty^2 t_\infty} \tag{17}$$

$$\dot{m}^+ = \frac{C_{prod}\tilde{\rho}_v (\alpha_l + \sum_{k=2}^{K}\alpha_k)^2 \alpha_v}{t_\infty}$$

$$p_v = p_v(T)$$

In the liquid-vapor mass-transfer model, the destruction of liquid is related to the difference of the local pressure, *p*, and vapor saturation pressure, p_{sat}, and the production of liquid. Within the context of Eq. 17, saturation vapor pressure is an assumed function of temperature; thermal effects on phase change can be included.

The model system is closed with the inclusion of equations of state for the constituent phases and species. For the liquid phase, for instance, $\tilde{\rho}_l = \tilde{\rho}_l(p,T)$ and $h_l = h_l(p,T)$. For the constituent gaseous species, including the vapor, the species density and enthalpy may be expressed similarly.

Generalized Equation of State

Within the context of the given model equations, a general state equation can be specified, for any species. This is useful for handling compressible simulations of liquid and gaseous phases. In this work, the state relations used are either an isothermal equation of state, given by

$$\tilde{\rho} \approx \tilde{\rho}_0 + (p - p_0)\frac{\partial \tilde{\rho}}{\partial p} + \cancelto{0}{(T - T_0)}\frac{\partial \tilde{\rho}}{\partial T} \approx \tilde{\rho}_0 + \frac{(p - p_0)}{a^2}, \tag{18}$$

or a temperature-dependent, state relation with a temperature dependent, linearized pressure effect is given by

$$\tilde{\rho} \approx \tilde{\rho}_0(T) + (p - p_0)\frac{\partial \tilde{\rho}(T)}{\partial p} = \tilde{\rho}_0(p_{sat}, T) + \frac{p - p_{sat}}{a^2(p_{sat}, T)}. \tag{19}$$

In the last relation, $\tilde{\rho}_0$ and *a* are both functions of temperature based along the saturation pressure curve. The form to the right is preferred as it is only a slight modification from the isothermal state relation, which is recovered by setting $\tilde{\rho}_0$ and *a* to constants. As the pressure deviates from p_{sat}, small errors tend to occur in the temperature behavior. However, the density is an explicit function of pressure and temperature, which provides a more computationally efficient state relation to represent complicated regimes. These two relations can reasonably represent the liquid and gaseous properties for the flows of interest. Finally, all fluid properties are gathered from Afeefy *et al*. [13]

RESULTS

Various flow types of cavitating-fluid flows are explored to ascertain their sensitivity to thermal cavitation. The applications examined include partially cavitating water flows, cryogenic flows, and heated flows that may be considered as boiling type flows.

Cavitating Water Flows

Several cavitating-water flows are investigated in regards to examining the sensitivities of thermal effects. The cases include a two-dimensional NACA 0015 hydrofoil, a three-dimensional twisted hydrofoil, and a three-dimensional, oscillating fin geometry.

NACA 0015

Simulations of the NACA 0015, based on the experiments of Cervone *et al.* [14], at various free-stream temperatures are performed. The temperatures examined are at T = 25, 50, and 70 degrees C, which displays a gradual increase in the thermal effect. In this study, the effect of modeling temperature-dependent fluid properties is examined. For future reference, we refer to temperature dependent changes of ρ(T), C_v(T), $a(T)$, and $e(T)$ as thermal-fluid properties. In the first case, or CFD1, the thermal-fluid properties are ignored, and are based on their values at the free-stream conditions. Note that despite eliminating the thermal-fluid property relations, the saturation pressure remains a function of T, or $p_{sat}(T)$, to retain such effects. This is compared to a second case, CFD2, that accommodates the thermal-fluid properties with Eq. 19, using approximations to data reported by Afeefy *et al.* [13]. These approximations are based along the saturation curve. If differences in the solutions are observed, modeling the fluid properties can be assumed to be important.

The computational grid is an overset-mesh system based on the experimental setup described by Cervone *et al.* [14]. A two-dimensional mesh is used in this analysis. The hydrofoil uses a 299x29 O-grid, with y^+ values of 10. The wall mesh extends 0.3 m upstream of the hydrofoil quarter-chord and 0.35 m downstream. The vertical positioning was not specified for the experiments, thus, it was assumed that the foil was vertically centered about the quarter chord within the tunnel. The upstream total pressure was specified along with a down-stream static pressure. Note the small discrepancy in the CFD definition of cavitation number that is based on the outlet pressure, as compared to the upstream pressure as used by Cervone *et al.* [14]. The conditions are $Re_c=5x10^5$, varied σ values, and varied temperatures. These cases all use an unsteady, k-ε RANS formulation.

The predicted mean, minimum, and maximum cavity lengths are used to assess the unsteady cavity characteristic. These cavity lengths are also reported by Cervone *et al.* [14], which are based on visual measurements. Such comparisons can be difficult using computational solutions, as CFD yields quantities such as density and/or volume fraction, which does not necessarily correlate well with a visually observed interface. For example, the mean density used to define the location of a sheet cavity is obviously given by the vapor density. In cloud cavitation, the cavity definition is not so obvious. The mean density describing the cavity length is an arbitrary number between the vapor and liquid densities, of which is not constant. Regardless, we base the cavity length on the isosurface of 0.05. Lastly, additional uncertainties present themselves using a two-dimensional model, on what becomes a highly three-dimensional flow. Considering these difficulties and modeling uncertainties, our goal is to quantify the effect of temperature variations in the fluid properties; thus, qualitative agreement justifies the validity for such assessments.

The trends of the predictions using the CFD2 method, across the varied temperatures, are compared to the experimental measurements in Fig. **1** below. The plot only displays the maximum cavity length. Note that the maximum length at a low cavitation number was the basis for the choosing the α_v=0.05 isosurface as a representative cavity length. The trend between the experiment and CFD solutions are in good agreement. At low cavitation number, the data and predictions match well as expected based on how the cavity length was determined. In the mid-range cavitation numbers, the cavity length displays a region of large length increase when σ is decreased, or a sharp drop in $dL/d\sigma$. Experiments display a trend that delays this behavior at lower temperatures. A similar trend is captured using CFD, however offset to a lower σ. Approaching the high σ values, the CFD curves converged, in a similar behavior as do the experiments. Although the CFD solutions do not predict identical behavior to the experiments, which can be attributed to an ambiguity in the cavity length definition as well as the lack of three-dimensional models, the trends are captured well enabling validity in the upcoming assessments.

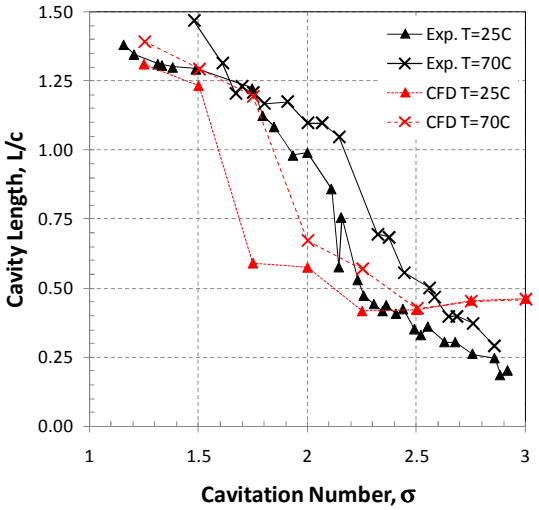

Figure 1: Comparison of simulations (CFD2) to experimental observations of the unsteady cavity lengths from Cervone *et al.* [14] at varied free-stream temperatures and α=8°. Note that the CFD cavity length is defined by the vapor-volume fraction of 0.05 isosurface.

Comparisons of the predicted versus experimental cavity lengths at T=25° C are given in Fig. **2**. The trends remain in reasonable agreement, however, the qualitative agreement is correct. The cavities display strong unsteadiness at the cavitation numbers where the minimum and maximum curves diverge. The CFD and experiments agree well in this region. However, the mean cavity length is lower than observed. For σ > 2.25, the cavity is steady and the predicted trend is slightly high and with a negative slope. As before, the issues with the CFD predictions are attributed to determining the cavity length. In comparing the effect of the fluid property definitions, by comparing the CFD1 and CFD2 curves, little difference is observed. This implies a lack of importance in resolving the thermal-fluid properties for thermally insensitive cavities.

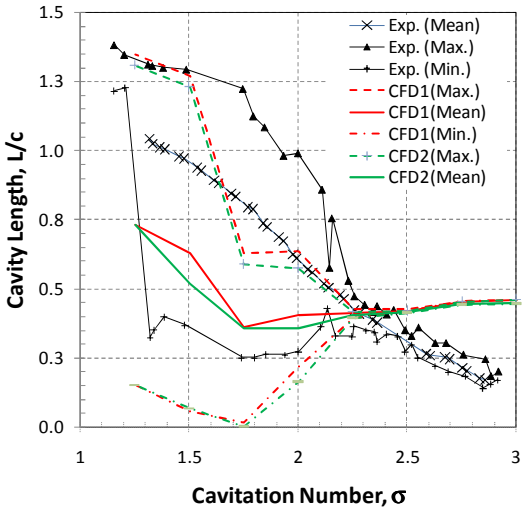

Figure 2: Comparison of simulations to experimental observations of the unsteady cavity lengths from Cervone *et al.* [14]. Fluid-state properties are only *p*-dependent for CFD1, and *p* and *T* dependent for CFD2. Note that the CFD cavity length is defined by the vapor-volume fraction of 0.05 isosurface. The conditions are at α=8° and T=25°C.

To consider the effect in warm water, where the properties are more sensitive to temperature changes and the temperature drops are expect to be increased, the T=70° C case is considered. This is provided in Fig. **3**. In general, the agreement with experiment is similar to the T = 25° C case. Again, the CFD1 and CFD2 solutions agree well with each other. This suggests that even at this increased temperature, where the fluid properties are more sensitive to the thermal effects, the thermal-fluid properties have a negligible effect on the predictions.

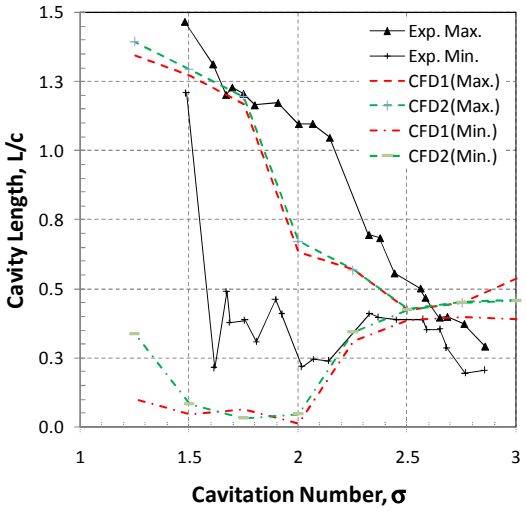

Figure 3: Comparison of simulations to experimental observations of the unsteady cavity lengths from Cervone *et al.* [14]. Note that the CFD cavity length is defined by the vapor-volume fraction of 0.05 isosurface. The conditions are at α=8° and T=70°C.

Lack of modeling thermal influences on ρ(T), C_v(T), *a(T)*, and *e(T)* can dramatically increase the code performance. The fact that theses cavitation predictions display little sensitivity to their modeling, suggests that they have a minimal impact. The major effects are captured in the $p_{sat}(T)$ relation combined with the free-stream fluid properties, or ρ_∞, $C_{v,\infty}$, a_∞, and e_∞. This of course, is limited to cavitation modeling without added heat sources. In any case, CFD algorithms often require many solutions to state relations and obtaining other fluid property definitions. Thus, simplifications in these equations can correspond to significant code-speed reductions. Based on these results, considering complex equations of state or interpolation tables of fluid properties [5] may be nonessential for thermal cavitation simulation.

Delft Twisted Hydrofoil

The influence of handling the state-equation terms, within the modeling approach, is evaluated for more complicated three-dimensional hydrofoil geometry. The geometry is based on a NACA 0009 hydrofoil, and has a varied twist from 0 to 11 degrees along the span of the geometry. The model is representative of the experiments of Foeth *et al.* [15] and Foeth [16], which is intended to reproduce cavities similar to those observed on propulsors.

The simulated conditions remain close to the experimental conditions. The cavitation number, σ, is 1.07, and the Reynolds number, Re_c, is 1.146×10^6. In these simulations, the water density, ρ_l, remains near 1000 kg/m^3, and the vapor density, ρ_v, roughly 0.1 kg/m^3. Note that the prescribed ρ_v is roughly four times higher than actual at room temperature, which is considerably less than standard practice suggests (ρ_v = 1.0 kg/m^3) [17], but still four times higher than actual. These simulations use a *k*-ε-based DES approach, with appropriate mesh spacing and time-step sizes. The computational mesh used throughout these studies can be referenced in Kinzel [18]. The mesh assumes a plane of symmetry along the centerline, and uses a wing-conforming C-grid (366x214x39) and a tunnel-resolving Cartesian grid (125x51x21). Note that Kinzel [18] performed some analysis of mesh independence, which displayed that additional resolution is needed. However, in such a comparative study, conclusions can still be drawn and the trends should valid.

Predictions using various energy-equation assumptions are compared to the experiments in Fig. **4**. In this comparison, the mean cavity behavior is displayed. The CFD solutions are based on time-averaged flow fields. The experimental average is generated by an averaging of the images of a video sequence using ImageMagick® [19]. The dotted lines outline regions of the average experimental cavity; specifically, the red line outlines the mean cavity location and the yellow line distinguishes the foamy and sheet cavity regions. This is useful for evaluating the different CFD solutions. In the CFD solutions, two isosurfaces at vapor-volume fractions of 0.7 (dark blue) and 0.3 (light blue) are used to represent the sheet- and foamy-cavity regions, respectively.

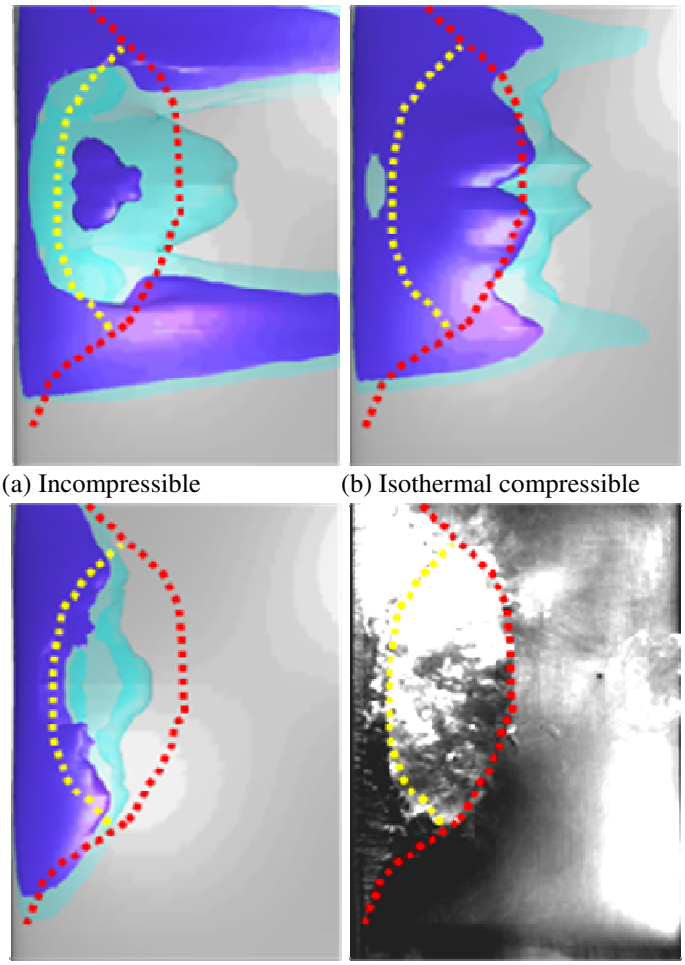

(a) Incompressible (b) Isothermal compressible

(c) Fully populated energy eqn. (d) Experiment video [16]

Figure 4: Comparison of the DES simulations using various state equation assumptions to an experimental video compressed into a single image. The cavity from the experiment is outlined by the red-dashed line and the mixture region is indicated using the yellow-dashed line. The dark-blue and light-blue isosurfaces are at α=0.7 and α=0.3, respectively.

In observing Fig. **4**, the handling of the compressible behavior appears to be important for predicting the correct cavity shape. A solution using incompressible assumptions displayed in Fig. **4** (a), which is achieved by assuming that $a=\infty$, using the state equation defined in Eq. 18, and ignoring thermal effects. Here, a similar-to-experiment mean-cavity structure is observed, however, overly vaporous coat-tail-like structures and a lack of predicting a cavity that extends span wise are cavity characteristics missed in this prediction. The solution that uses an isothermal compressible model is achieved using similar assumptions, however, a is set to finite values [13] based on the liquid and vapor phase values. The solution is pictured Fig. **4** (b) and displays similar features as does the incompressible case, but, the deficiencies are improved compared to the experiment. Using a fully populated energy equation and accounting for fluid property thermal effects using Eq. 19, the solution is provided in Fig. **4** (c). Relative to experiments, significant improvements are apparent when energy conservation is maintained. The cavity now correctly extends in the span-wise direction, the sheet-cavity length and foamy regions correspond well with the experiments, and the coat-tail structures are eliminated for the vapor-volume fractions shown. Such improvement gives promise in the ability to predict cloud-cavitation problems using energy-conserving CFD. Despite improvement in the cavity shape, the forces in each case were roughly the same.

Oscillating, Cavitating Fin

Further effects on the energy-equation modeling approaches are observed in the time-accurate predictions of an oscillating fin (The fin aspect ratio is 4 and the profile is based on a proprietary 0.15t/c hydrofoil). These cases similarly use a k-ε DES formulation. The oscillation cycle can be extracted from the dashed line of Fig. **5** (a) in the figure below. Although the reduced frequency in this case suggests a quasi-steady flow based on single-phase measures, in the cavitating-fluid condition the dynamic response of the cavity is rather slow creating dynamically pitched unsteady conditions. Note that these simulations are based on the experiments presented in the work reported by Kinzel *et al.* (performed by Willits. S.) [20], however, are simulated at an increased reduced frequency to reduce the simulation time. Comparisons of the predicted lift and the lift-power spectra are displayed below for various models of the state equation in Fig. **5** (a) and (b), respectively. In Fig. **5** (a), the nonharmonic fin oscillation cycle is plotted for comparison purposes. The pitch cycle is also displayed in terms of a lift-power spectra in Fig. **5** (b), using finite-wing theory to co-plot the magnitudes. Although the mean loads are quite similar, significant differences in the high-frequency fin loading (apprant in Fig. **5** (b)) suggest that maintaining a fully populated energy equation is required if studying effect important at those frequencies. Additional differences can be observed in the pitching-moment predictions, in Fig. **5** (a), and is even more apparent in the bending-moment predictions and Fig. (b). The combined differences indicate that cavity dynamics and the resultant high-frequency loading events are best captured with the energy conservation. Thus, the computation of acoustic sources, vibrational loads, and cavitation damage will all likely rely on such model improvements.

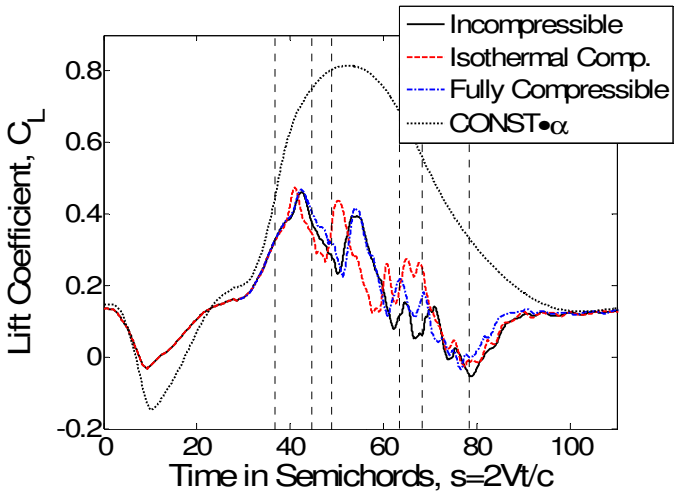

(a) Lift Vs. time

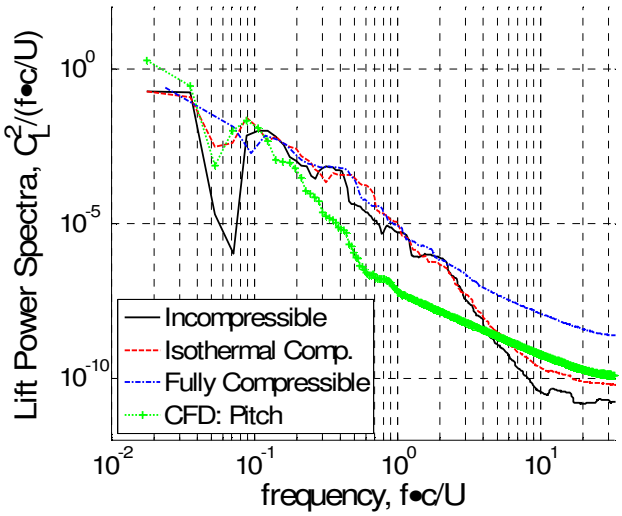

(b) Lift-power spectra Vs. frequency

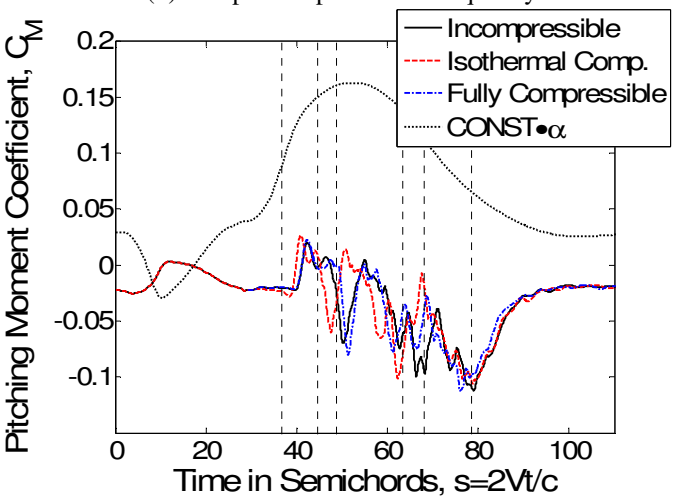

(c) Pitching moment Vs. time

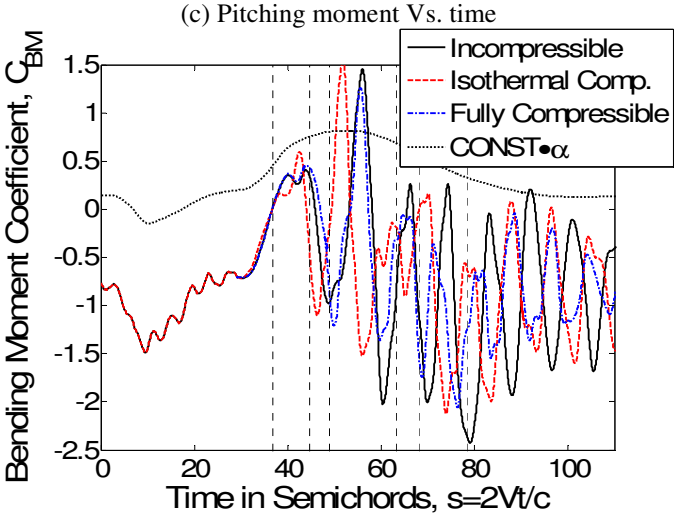

(d) Bending moment Vs. time

Figure 5: Comparison of the lift and moment predictions through an oscillation cycle and the corresponding lift-power spectra using various state-equation assumptions.

Comparisons to the experimentally observed and predicted cavities are displayed in Fig. **6**, with comparisons of the solutions using an incompressible, isothermal-compressible, and full energy-conserving-compressible models. Each instance is displayed sequentially, and can be referenced as indicated in the load prediction plots of Fig. **5** using the vertical-dashed lines. Note that additional details of these predictions are available in the thesis of Kinzel [18]. In all cases, as the cavity initially develops, the cavity remains stable and has a well-defined structure as apparent in Fig. **6** (a). All cases uniformly predict this behavior, a similar shape and cavity curvature approaching the tip, as well as the cavity interacting with the water-tunnel wall at the fin-wall junction.

At a later instance, just after the cavity extends past the trailing edge of the fin, the cavity destabilizes. This feature is observed in Fig. **6** (b). All of the simulations display cavities that are in agreement with the experiment, however, time synchronization with the experiment was not performed due to lack of information from the experiments. Note that the simulations are, in fact, displayed at consistent times. In general, the simulations are all in reasonable agreement with each other. Advancing through time, through Fig. **6** (d), the pitch angle is still being increased and the experiments and simulations continue to display similar cavity shapes. The comparisons between the simulations, however, tend to deviate from each other based on varied cavity dynamics. This variation in the unstable cavity dynamics continues to be the major effect of the including the energy equation. Not only does this affect the high-frequency cavity dynamics, one would expect that as the pitch oscillations increase in frequency near the shedding frequency, the loads will be dominated by energy-equation sensitive features. This is not the case for this lower frequency, k~0.05, oscillating case.

As the fin pitches downward, in Figs. **6** (e) and (f), secondary shedding events and eventually recovery from the cavitation event occurs. These cases display many cavity scales, and in general, agree well with the experiments. There are obvious differences between the solutions and experiments that are likely a combined effect of varied oscillation frequency, and lack of an ability to reference the photograph with a specific pitch angle. Comparing the predictions also displays differences due to the varied cavity dynamics that can be attributed to the thermal effects. This is consistent with the previous observations, however, the cavity is less coherent.

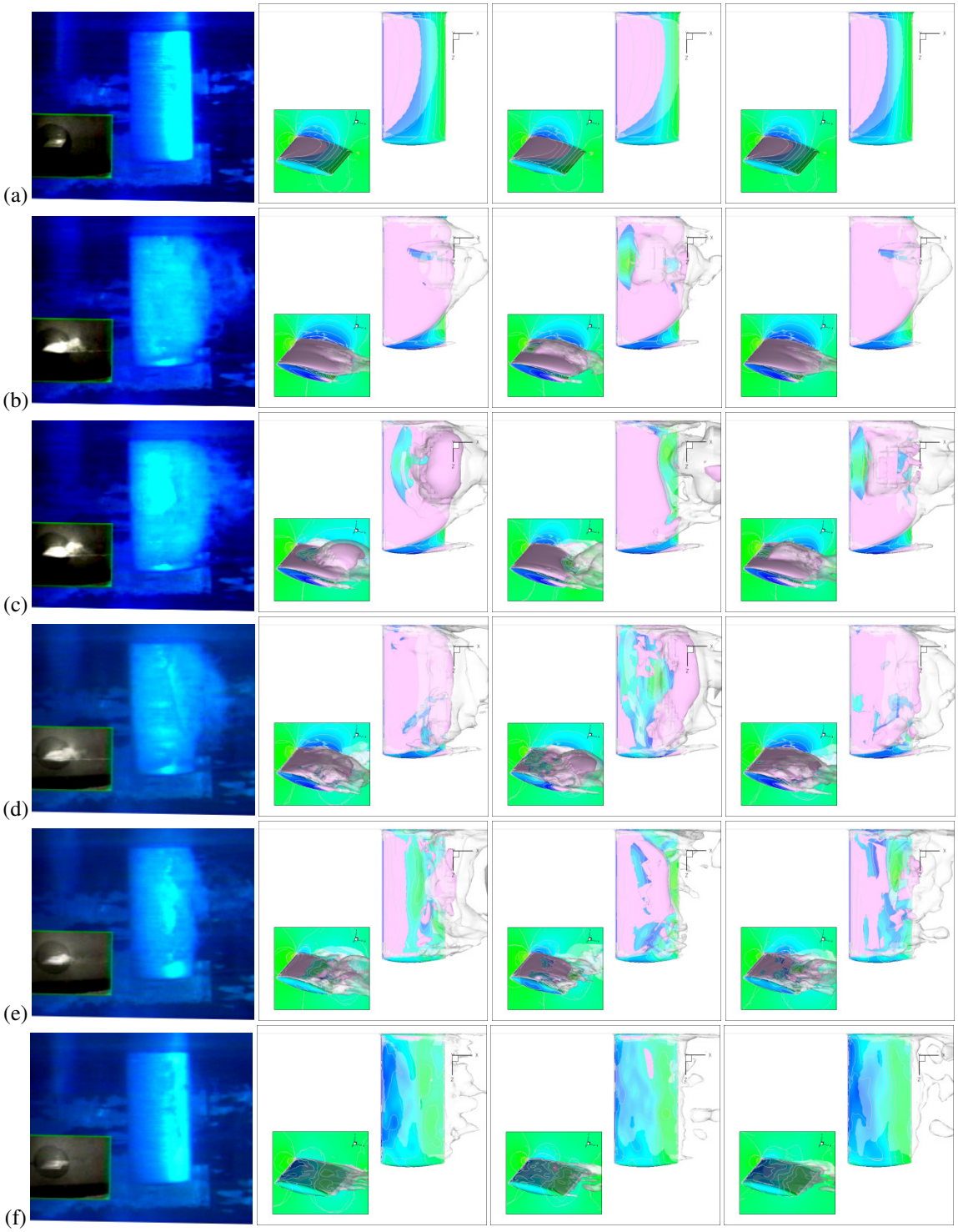

Figure 6: Comparisons of state equation assumptions and experiments during the initial cavity cycle. The columns, from left to right, respectively display the cavities observed in experiments (Kinzel *et. al.* [20]), incompressible, isothermal compressible, and full energy conserving compressible with $p_{sat}(T)$. All cases use the DES turbulence model. The pink and translucent white isosurfaces represent the $\alpha = 0.5$ and 0.1 values, respectively.

Cavitating Cryogenic Flows

Strongly coupled thermal effects and phase change are found in the flow of cryogenic fluids. As has been noted by others, the sensitivity of saturation vapor pressure to small changes in temperature coupled with the usual effect of latent heat make thermal considerations critical to modeling of cryogenic cavitation [2] [5]. This case represents a physical experiment conducted and reported by Hord [2] and previously

studied using a RANS model by Hosangadi and Ahuja [5]. The flow of liquid nitrogen over a hydrofoil is modeled in a cryogenic flow tunnel (case 290C in Ref. [2]). A photograph from Hord [2] of an unsteady vaporous cryogenic hydrogen cavity attached to the same hydrofoil is shown in Fig. **7** (a). Although Hord only presented select photographs of cryogenic hydrogen flows Fig. **7** (a) is representative of the general qualities of the flows under consideration, namely attached, cryogenic cavity flows over a zero camber, 2-D hydrofoil. The hydrofoil section was 6.35 cm long and set at zero angle-of-attack. From the experimental results, the Reynolds number for this case, based on chord length, was 9.1 million.. The absolute upstream temperature was 83.06K, the pressure was 568.3kPa, and the mean inflow was given as 23.9m/s. The cavitation number was 1.7 and referenced to an upstream probe where the measured vapor pressure was 188.6kPa. For this case, an attached cavity forms over the hydrofoil. From the reported results, the actual level of unsteadiness in the experiments is unclear. However, as is typical of vaporous cavities closing on solid surfaces, Hord indicated that the aft half of the cavities studied was generally unsteady. This made accurate experimental determination of cavity lengths difficult [2].

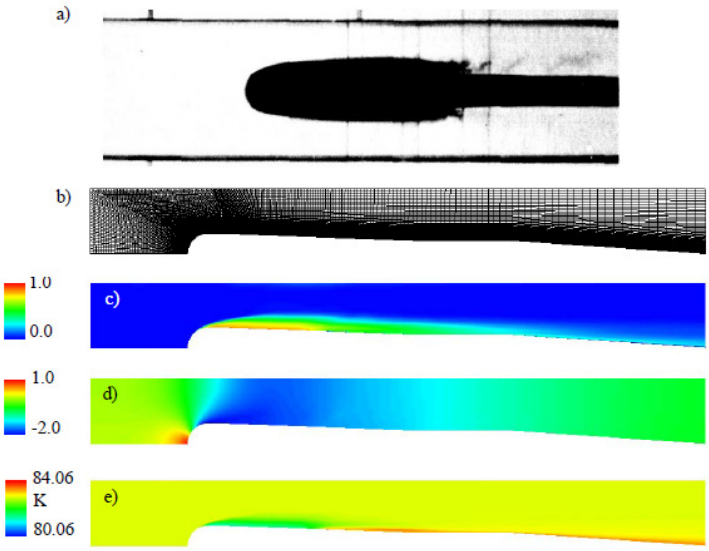

Figure 7: Experimental [2] and modeled cryogenic hydrofoil flows. Modeled flow time averaged and is of nitrogen at σ=1.7 and Re_C=9.1 million with upstream at 83.06K, 23.06m/s, and 568.3kPa.
(a) Photograph from testing (hydrogen at unknown conditions).
(b) Computational grid of modeled domain.
(c-e) Vapor volume fraction, pressure coefficient, and temperature from computed solution

The 2-D grid of approximately 30,000 cells used to obtain the present results is shown in Fig. **7** (b). The fluid properties from Afeefy et al. [13] were used to model cryogenic Nitrogen. To obtain the modeled results, the inflow total conditions were held constant while the back pressure was adjusted to obtain the desired conditions. As a result, the (time-averaged) model inflow velocity at the probe location was actually 23.06m/s. Photographs and description of the physical experiment suggest an unsteady, three-dimensional flow field. However, since the purpose of this investigation is mainly to demonstrate physically sensible thermal effects coupled to flow-induced phase change, the flow was modeled as two dimensional. In the experiment, aft of the foil section, a somewhat complex three-dimensional support sting supported the hydrofoil. In computational modeling, aft of the hydrofoil section, a gradually tapered tailing edge was substituted. With coarse grids the modeled flow appeared steady. However, when sufficient resolution was applied to resolve the cavity, as determined by cavity size and magnitude of temperature depression, converged steady-state integrations were difficult to obtain. Thus, results presented here were obtained with time-accurate integration but applying two-dimensional physics and RANS.

In Fig. **7** (c) the time-averaged computed cavity size and shape are presented via the vapor volume fraction contour plot. In Fig. **7** (d), the pressure field is given and in Fig. **7** (e) the average temperature field is given. These time averages appear to agree with the expected tendencies in a cavitating flow field where the thermal effect is strong. In particular, the vaporization and the temperature depression effects tend to counteract each other resulting in a reduced vapor pressure and shorter cavity length. One shortcoming of the numerical results is the magnitude of temperature recovery downstream of the cavity. This is evident in Fig. **7** (e) where a slight overshoot above the free stream temperature appears to persist in the wall boundary layer due to unsteady reentrant mixing in the wake.

For illustrative purposes, snapshots from the unsteady flow field are presented in Fig. **8**. A single cavity cycle, over approximately 0.25ms is shown. Here the reentrant flow is seen to drive a cycle that is quite evident in both the pressure and volume fraction fields. The two-dimensional shedding of the computed cavity seems to be spatially segmented into waves. The waves are fed by gradually vaporizing liquid from beneath coming the aft end of the cavity and shed vapor tail of the cavity into the fine-grained, wispy mixture of liquid and vapor in the cavity wake. One might anticipate that full three-dimensional LES or DES turbulent simulations are required to capture the detailed flow features [22], but, the present simulations qualitatively capture the thermal interactions in the cryogenic cavity flows.

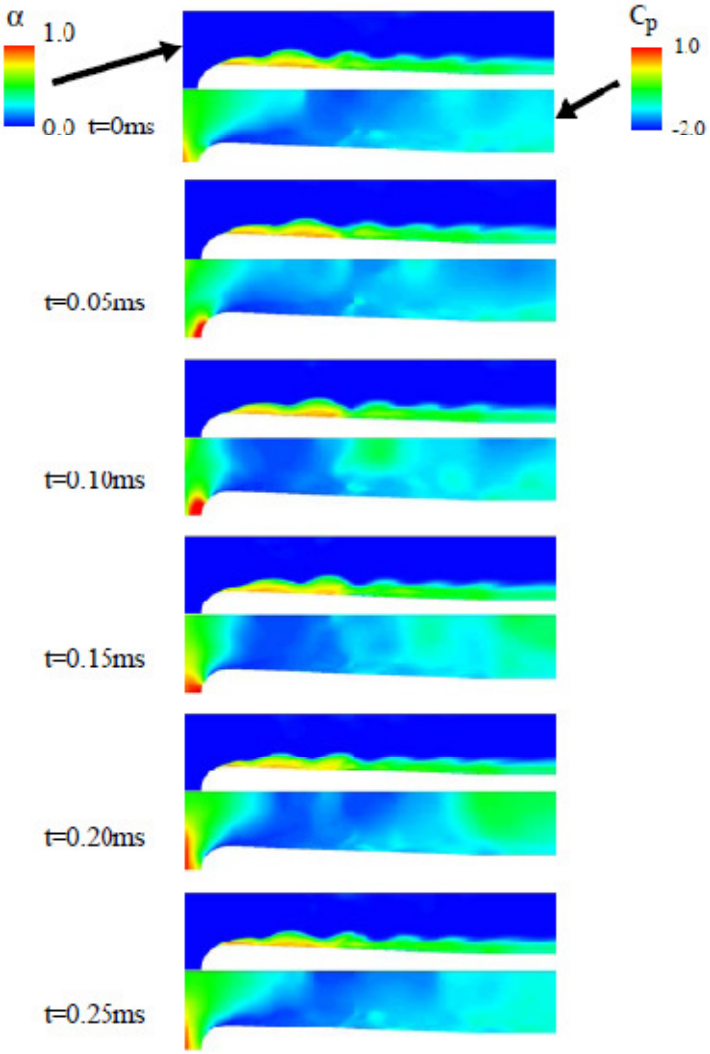

Figure 8: Snapshots from approximate computed cavity cycle: Cryogenic nitrogen flow over a hydrofoil. Vapor volume fraction and pressure coefficient are shown.

In Fig. **9**, the solution of modeled flow is presented alongside data from the experiments of Hord [2]. The experimental data is given in the form of average pressure and temperature measurements on the surface of the foil. The length of the experimental cavity was reported by Hord to be 1.9cm. This is the distance from the minimum pressure location to the point of approximate cavity termination. In the plots of Fig. **9**, the mean computed values, the extrema of the unsteady integration, and the standard deviation of the unsteady integrated properties over approximately 19 converged cavity cycles, of 0.26ms each, are shown. The duration of the integration sample used to construct these results was 5.0ms of modeled time, and the time step size was 0.5μs. This sampling was conducted after solution convergence at a statistically stationary condition. The level of computed unsteadiness is quite large. However, the greatest unsteadiness is not locally coincident for the temperature and pressure fields. The unsteadiness in these properties, found on the foil surface, is exhibited with the standard deviation shown in part (d) of Fig **9**. This plot tends to reinforce the appearances given by the plots of local extrema in parts (a) and (b). The magnitude of the standard deviation indicates a persistent unsteadiness reflected by the large local differences between the extrema and the mean values. The temperature is most unsteady in the region of high vapor volume fraction (inside the cavity) with pronounced peaks in local unsteadiness at the initiation and closure regions of the cavity. On the other hand, the pressure is very unsteady on the stagnation portion of the foil but appears steady, equal to the vapor pressure, inside of the mostly vaporous cavity. Thus there was an oscillatory pressure throughout the modeled test section driven by cavity cycling. This does not seem surprising given the large unsteady blockage; the test section height is 2.54cm, and the foil thickness is 0.792cm. As is the case in hydrodynamic cavitation, within the vaporous cavity, due to the relatively low density of the vapor, and the persistence of a high vapor volume fraction throughout the cavity cycle, there are negligible dynamics in pressure.

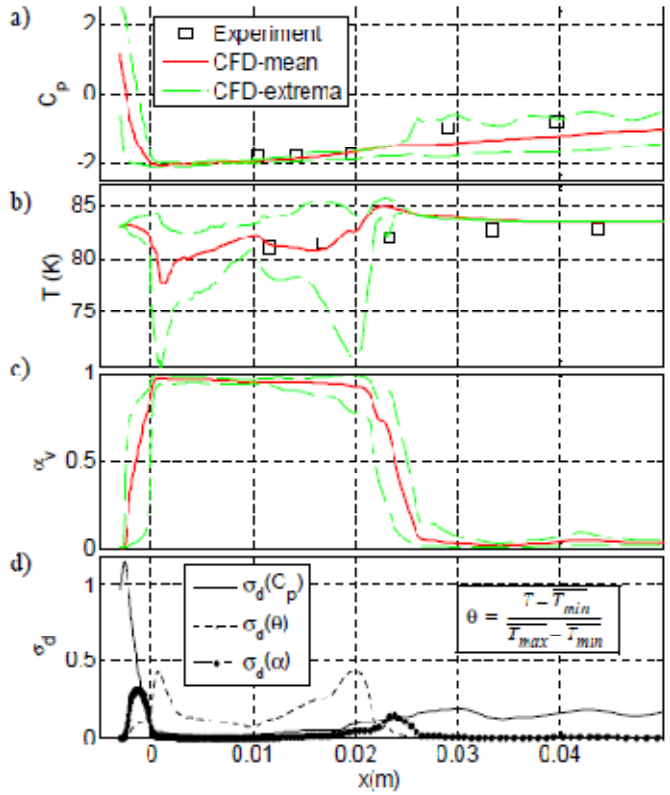

Figure 9: Properties on surface of foil. Experimental [2] and modeled cryogenic hydrofoil flows. Flow is nitrogen at cavitation number, σ=1.7, and Re_C=9.1 million with upstream conditions at 83.06K, 23.06m/s, and 568.3kPa. Axial distance (x) is given from location of minimum pressure.
(a) Pressure coefficient, modeled average and extrema, with experimental values.
(b) Temperature, modeled average and extrema, with experimental values.
(c) Vapor volume fraction, average and extrema.
(d) Standard deviation of modeled flow properties. Pressure coefficient, temperature coefficient,

Heated Applications

There are many cases where heating a liquid becomes dominate driver in the cavitating flow. Such cases obviously require energy-equation conservation modeling, thus, are highlighted to present motivating applications to include such modeling.

Shock-Wave Reflection

An example of shock-wave reflection inducing cavitation, or perhaps boiling, is given. The case is based on a sample problem described by Osher and Fedkiw [21], where a high-speed shock wave moving at $M=11.38$ strikes a gas-water interface. The domain is 10 m long, with x ranging from -5m to +5m. The initial gas-water interface is located at $x=0$ with gas at $x<0$ and water at $x>0$. This case initially has four separate regions: for $x<-4.04$, $\rho= 8.27\ kg/m^3$, $p=1.0\times10^7\ Pa$, $u=2950\ m/s$; for $-4.04\ m<x<0.0\ m$, $\rho=1\ kg/m^3$, $p=1.0\times10^5\ Pa$, $u=0\ m/s$; for $0.0\ m<x<4.62\ m$, $\rho=1000\ kg/m^3$, $p=1.0\times10^5\ Pa$, $u=0\ m/s$; and for $x>4.62\ m$, $\rho=1004.1\ kg/m^3$, $p=1.0\times10^7\ Pa$, $u=-6.38\ m/s$. The computational mesh applied contains 500 cells. The gas is modeled with the ideal-gas law ($\gamma_g=1.25$, $C_{v,g}=718\ JKg^{-1}K^{-1}$), whereas the liquid uses an isothermal equation of state for water based on Eq. 18 with $\rho_l=1000\ kg/m^3$, $a_l=1500\ m/s$, and $C_{v,l}=4130\ JKg^{-1}K^{-1}$. The liquid is allowed to vaporize and also uses the ideal-gas law with $\gamma_v=1.33$, $C_{v,v}=1452\ JKg^{-1}K^{-1}$.

The solutions at a time of 3 ms are compared in Fig. **10** for the (a) pressure, (b) velocity, and (c) temperature. Note that the vapor-volume fraction is plotted on the right axis to display where the phase change occurs. The amount of vapor formed is indicated by the deficit of the two curves. In this problem, without considering the effects of phase change, the solution is drastically different. In the case of an underwater blast or shock analysis, the need for such an analysis is obvious. For example in Fig. **10** (a), the impact of the vaporization process predicts that the resulting pressure magnitude doubles with vaporization. As well as the reflected shock, back into the air, is slower, cooler and also at an increased pressure. Such analysis requires an analysis similar to a cavitating-code capability, with an energy-equation conserving form.

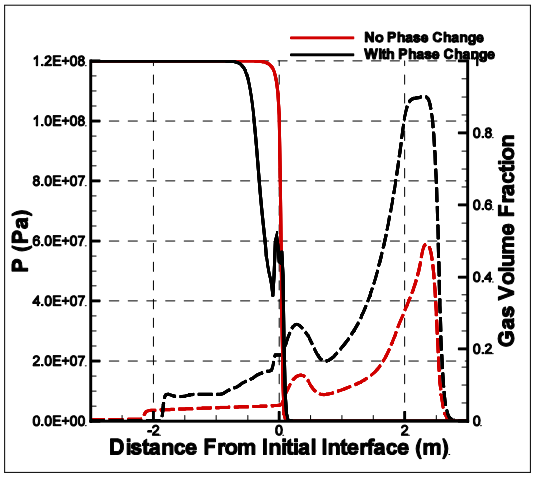

(a) pressure

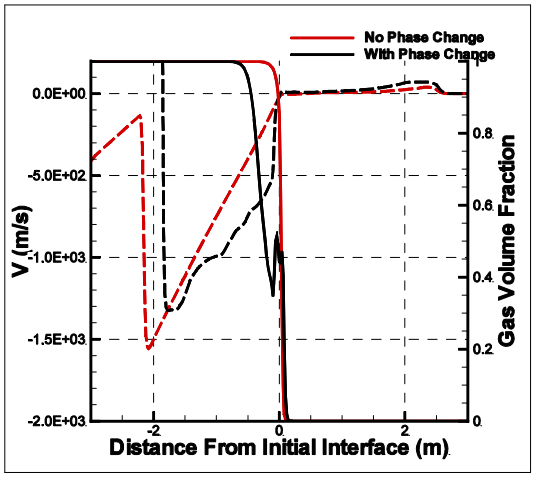

(b) Velocity

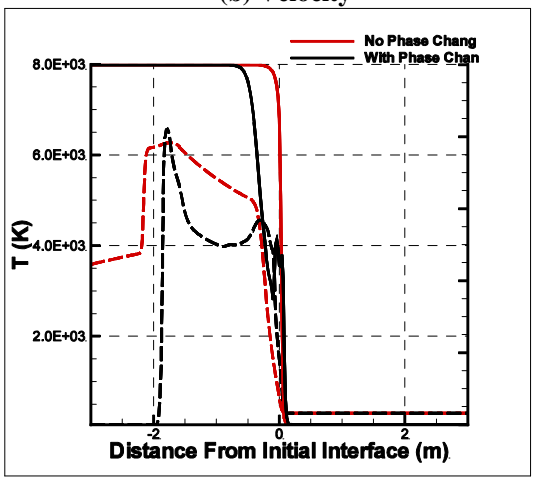

(c) Temperature

Figure 10: Solution at 3 ms after a Mach 11.38 shock wave strikes a gas-water interface. The liquid is allowed to vaporize through via boiling for the black lines, whereas this is suppressed for the red lines. Note that the dashed lines represent the left axis, while the solid lines represent the gaseous volume fraction.

Blasting Projectile

Finally, the application of thermal modeling is displayed on an underwater projectile launch. The projectile is blasted from a tube into water using high-temperature, high-pressure gas as displayed in the lower diagram of Fig. **11**. Above the diagram, in Fig. **11**, are contour plots of the axisymmetric simulation. This simulation is run using laminar-flow assumptions. From top to bottom, the vapor-volume fraction, α_v, the volume fraction of the heated/pressurized blast gas, α_g, and the temperature, T, are respectively plotted. It is apparent that the gas fills the projectile wake with a supercavity. This heated gas, along with the low pressures on the cavitator, boil the surrounding liquid water flow and fill the cavity with a gas-vapor mixture. This vaporization tends to cool the near-body cavity quickly, where more than a 500 K drop is observed. This particular test problem is just an example of additional physical behaviors that can be examined using thermal modeling.

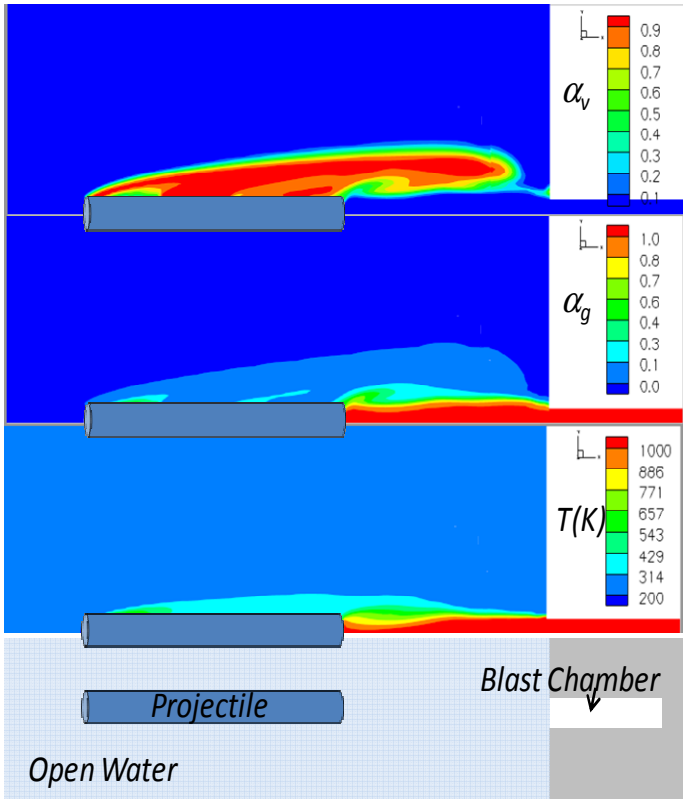

Figure 11: Solution of a projectile launch that is roughly one-projectile length outside the launch tube from which it was blasted.

CONCLUSION

In this work, we display that thermal modeling in cavitation can be important, but is highly dependent on the specific goal of the analysis. For typical hydrodynamic simulations, namely water flows at relatively low temperatures, incompressible and/or isothermal formulations are likely adequate. We have displayed that the first-loading mode, and the general cavity shape, appear to be relatively insensitive to thermal effects. This occurred for both steady and dynamic geometries, indicating that most hydrodynamic purposes need not include thermal modeling. As cavity-shape sensitivities appear to require thermal effects, the rather settle changes do not dramatically impact the steady or lower-frequency loads. However, the high-frequency content appears to be dependent on the capture of the thermal effects, suggesting that thermal modeling is a crucial component when the goal of the CFD is used for vibrational analyses, determining acoustic sources and perhaps propagation, and cavitation erosion. Furthermore, as high-frequency content displays the strongest influence, turbulent simulation techniques such as detached- and large-eddy simulation methods may require such modeling to remain relevant. Lastly, more obvious applications exist that without a doubt, require accounting for thermal effects within the simulations. These include cavitation in cryogenic flows, high-speed shock events leading to vaporization, and interactions between hot gases that boil off surrounding liquid flows.

Several studies of the state relations and/or fluid-property modeling were investigated. We display that improved fluid modeling has little impact to the analysis, indicating that the main factor in thermal modeling is driven by altering the saturated vapor pressure due to latent-heat-driven temperature changes. We also display moderate improvements in isothermal conditions using isothermal-compressible models, however, maintaining a fully populated energy-equation further affects the predictions.

As there is clear need for thermal modeling, improved algorithms and models are still clearly needed. Such improvements include algorithm speed and perhaps considering multi-fluid models that account for sub-grid scale slip along the cavity boundaries. Although incompressible flow models displayed slight deficiencies, which is somewhat due to dropping the temperature dependence in p_{sat}, such relations could be reintroduced. For example, perhaps $p_{sat}(\alpha)$ could correlate to $p_{sat}(T)$ as done in estimations of temperature drops within a cavity [4]. Such a method could reduce the simulation time, by equation reduction, and could still yield useful high-frequency analysis. In any case, the chosen numerical scheme will likely continue to be determined by the most efficient/effective method to analyze the specific problem at hand.

ACKNOWLEDGMENTS

This work was supported by the Office of Naval Research, under contract #N00014-07-1-0134, with Dr. Kam Ng as contract monitor, and contract #N00014-05-1-0435, with Dr. Judah Goldwasser program manager, overseen by William M. Hinkley and Thomas J. Griffen of the Naval Surface Warfare Center-IHD. Furthermore, much gratitude is given to Dr. David Hill, Dr. Mark Maughmer, Dr. Phillip Morris, and Dr. Ralph Noack of The Pennsylvania State University for their comments and insights added with respect to this work.

NOMENCLATURE

a	speed of sound
c	chord length
C_p	specific heat at constant pressure
C_v	specific heat at constant volume
e	internal energy
L	cavity length
p	pressure
p_{sat}	saturated vapor pressure
Re	Reynolds number. $\rho VL/\mu$
T	Temperature (C K)
V	velocity

Greek Symbols

α_g	volume fraction of noncondensable gas
α_g	volume fraction of vapor
μ	molecular viscosity
ν	dynamic viscosity
ρ	density
σ	cavitation number, $(p_\infty - p_{sat})/q_\infty$

Subscripts

c	reference to chordal properties
v	reference to vapor properties
l	reference to liquid properties

∞ reference to free stream

REFERENCES

[1] Stepanoff, A.J., "Cavitation in centrifugal pumps with liquids other than water," *Journal of Engineering Power*, Vol. 83, 79-80, 1961.

[2] Hord, J., "Cavitation in Liquid Cryogens–II. Hydrofoil," NASA CR-2156, 1973.

[3] Billet M.L. "Thermodynamic effects on developed cavitation in water and Freon 113" Master of Science Thesis, The Pennsylvania State University, March 1970.

[4] Franc, J.-P., Michel, J.-M., *Fundamentals of Cavitation*, Kluwer Academic Publishers, 2004.

[5] Ahuja, V., Hosangadi, A., and S. Arunajatesan, "Simulations of cavitating flows using hybrid unstructured meshes," *Journal of Fluids Engineering*, 2001, Vol. 123, No. 2.

[6] Lindau, J.W., Venkateswaran, S., Kunz, R.F. and C.L. Merkle, "Development of a fully-compressible multiphase Reynolds-averaged Navier-Stokes model," AIAA 2001-2648, 2001.

[7] Venkateswaran, S. and Merkle, C.L., "Analysis of preconditioning methods for the Euler and Navier-Stokes equations, Von Karman Institute Lecture Series," 1999-03, March 1999.

[8] Li, D., Sankaran, V., Lindau, J.W., and C.L. Merkle, "A Unified Computational Formulation for Multi-Component and Multi-Phase Flows," AIAA Paper 2005-24906.

[9] Roe, P.L., "Approximate Riemann solvers, parameter vectors, and difference schemes," *Journal of Computational Physics*, Vol. 43, 1981, pp. 200-212.

[10] Vinokur, M. and Liu Y., "Equilibrium Gas Flow Computations 11: An Analysis of Numerical Formulations of Conservation Laws," AIAA paper 88-0127, 1988.

[11] van Leer, B, "Towards the Ultimate Conservative Difference Scheme, V. A Second Order Sequel to Godunov's Method," *Journal of Computational Physics*, 32, 101–136.

[12] Strelets, M. "Detached eddy simulation of massively separated flows," AIAA paper 2001-0879, 39th Aerospace Sciences Meeting and Exhibit, Reno, Nevada, 2001.

[13] Afeefy, H.Y., Liebman, J.F., and Stein, S.E., "Neutral Thermochemical Data," *NIST Chemistry WebBook*, NIST Standard Reference Database Number 69, Eds. P.J. Linstrom and W.G. Mallard, June 2005, National Institute of Standards and Technology, Gaithersburg MD, 20899 (http://webbook.nist.gov).

[14] Cervone, A., Bramanti, C., Rapposelli, E., and d'Agostino, L., "Thermal Cavitation Experiments on a NACA 0015 Hydrofoil," *Journal of Fluids Engineering*, 128, 326 (2006), DOI:10.1115/1.2169808.

[15] Foeth, E.J., van Doorne, C.W.H., van Terwisga, T., Wieneke, B., "Time Resolved PIV and Flow Visualization of 3d Sheet Cavitation," *Experiments in Fluids*, Vol. 40 pp. 5030513, 2006.

[16] Foeth E.J., "The structure of three-dimensional sheet cavitation," Ph.D. Thesis, Delft University, 2008.

[17] Kunz, R.F. Boger, D.A. Stinebring, D.R. Chyczewski, T.S. Lindau, J.W. Gibeling, H.J. Venkateswaran, S. and Govindan, T.R., "A preconditioned Navier-Stokes method for two-phase flows with application to cavitation predication," *Computers and Fluids*, 29, pp. 849-875, 2000.

[18] Kinzel, M. P., "Computational Techniques and Analysis of Cavitating-Fluid Flows." Dissertation in Aerospace Engineering, University Park, PA, USA: The Pennsylvania State University, May 2008.

[19] ImageMagick, www.imagemagick.org

[20] Kinzel, M.P., Willits, S.M., Lindau, J.W., Boger, D.A., Kunz, R.F., Medvitz, R.B., Noack, R.W., "CFD Simulations of Oscillating Hydrofoils With Cavitation," AIAA Paper No. 2006-1039, 44rd Aerospace Sciences Meeting, Reno, NV, USA, January, 2006.

[21] Osher, S., Fedkiw. R., S., *Level Set Methods and Dynamic Implicit Surfaces*, Springer-Verlag New York, Applied Mathematical Sciences, 153, 2002.

[22] Lindau, J.W, Kunz, R.F, Sankaran, V, Stinebring, D.R. and L.J. Peltier, "Development and Application of Turbulent, Multiphase, CFD to Supercavitation," 2nd International Symposium on Seawater Drag Reduction, Busan, Korea, 23-26, May 2005..